# Genetically encoded mechano-sensors with versatile readouts and compact size

Yuan Ren[#,1,2*], Jie Yang[#,3], Takumi Saito[#,1,2,4], Oliver Glomb[5], Sayed Iman Mousavi[1,2], Brigitte Naughton[1,3], Christina de Fontnouvelle[1,3], Barbara Fujita[1,2], Christian Schlieker[1,3], Shaul Yogev[6], Yongli Zhang[1,3*], Julien Berro[1,2,3*]

1 Department of Molecular Biophysics and Biochemistry; Yale University, New Haven, CT, USA

2 Nanobiology Institute, Yale University; West Haven, CT 06516, USA

3 Department of Cell Biology, Yale University School of Medicine; New Haven, CT 06520, USA

4 Graduate School of Biomedical Engineering, Tohoku University, Sendai 980-8579, Japan

5 Institut für Klinische Anatomie und Zellanalytik, Medizinische Fakultät, Eberhard Karls Universität Tübingen; Österbergstraße 3, 72074 Tübingen, Germany

6 Department of Neuroscience, Yale University School of Medicine; New Haven, CT 06520, USA

# Equal contributions

*Corresponding authors. Email: yuan.ren@yale.edu, yongli.zhang@yale.edu, julien.berro@yale.edu

## Abstract

Mechanical forces are critical for virtually all fundamental biological processes, yet quantification of mechanical forces at the molecular scale *in vivo* remains challenging. Here, we present a new strategy using calibrated coiled-coils as genetically encoded, compact, tunable, and modular mechano-sensors to substantially simplify force measurement *in vivo*, via diverse readouts (luminescence, fluorescence and analytical biochemistry) and instrumentation readily available in biology labs. We demonstrate the broad applicability and ease-of-use of these coiled-coil mechano-sensors by measuring forces during cytokinesis (formin Cdc12) and endocytosis (epsin Ent1) in yeast, force distributions in nematode axons (β-spectrin UNC-70), and forces transmitted to the nucleus (mini-nesprin-2G) and within focal adhesions (vinculin) in mammalian cells. We report discoveries in intracellular force transmission that have been elusive to existing tools.

## Main

Currently there are two major categories of sensors to measure mechanical forces at the single molecule level for live biological samples. One uses DNA duplexes (hairpins) that rupture at different levels of force[1–3], and the other one utilizes elastic peptides (nano-

springs) that monotonically change their extension in a force-dependent manner[4–6] (Fig. 1a-b). Both are tuned to maximize their conformational change to tensile mechanical forces in the pico-newton (pN) range, and the conformational changes are commonly quantified by Förster Resonance Energy Transfer (FRET) measurements[7–10]. Variations of mechano-sensors based on these principles have had great successes and yielded valuable insights into the mechanical workings of cell attachment, cell motility, and embryo development[11–16]. Nevertheless, both approaches have inherent limitations in their broad applications. For the DNA duplexes, it is easy to tune their mechanical properties and alter readouts[17–20] (Fig. 1a). However, it is difficult to deliver DNA duplexes into cells and protect them from rapid degradation. Therefore, DNA duplexes are only applied to measure force on extracellular protein domains[10,21]. Mechano-sensors based on calibrated elastic peptides, on the other hand, can be genetically encoded within any protein of interest in theory. However, the inclusion of two fluorescent proteins for FRET measurement results in a large sensor size (>55 kDa) that is rarely tolerated by the host protein (Fig. 1b). Additionally, FRET measurements are inherently challenging to perform, requiring extensive controls and calibration. These measurements are highly context-dependent, time-consuming, and exhibit a moderate dynamic range (5-25%) *in vivo*[22–25]. Therefore, smaller genetically encoded mechano-sensors that do not rely on FRET measurements are desired to democratize molecular force measurements in cell and developmental mechanobiology beyond the few commonly studied molecules.

We present a new class of mechano-sensors that retains the programmable digital mechanical response and versatile readouts of DNA sensors, while being fully genetically encoded and substantially smaller than the current peptide-based force sensors[23,24] (Fig. 1c). We achieve this goal through a modular approach by building on force sensors we have previously developed[26–28]. The *force-sensing module* is composed of a dimeric anti-parallel coiled-coil that unfolds (i.e. fully opens) when the tensile force applied to it is larger than a calibrated force threshold. The *readout module* is bipartite and made of a) a peptide that links the two α-helices of the coiled-coil and b) an interacting partner that binds the linker only when the coiled-coil is in an open conformation but not when it is in a closed conformation (Fig. 1c). The binding between different linkers and their binding partners can be engineered to generate binary signals that are gated by the force on the coiled-coil (Fig. 1f). Due to its small size and short end-to-end distance (~13 Å, or the typical length of a 5 amino acid linker), the mechano-sensor can be placed at virtually any flexible region within a protein of interest between its domains with minimal influence on the protein's function.

We derived our library of force-sensing modules from an artificial heterodimeric antiparallel coiled-coil[29], which unfolds at 7.4 ± 0.1 pN (mean ± SEM) (Fig. 1d). Dimeric coiled-coils are stabilized by knobs-into-holes packing at the hydrophobic core along with electrostatic pairing on the surface[30,31]. We tuned the mechanical stability by 1) varying the amino acids in the hydrophobic core and 2) changing the total number of heptad repeats (Fig. S1). We also used molecular simulations to aid our design (Fig. S1). The resultant coiled-coils have the same end-to-end distance and surface properties when

folded, and each sensor reversibly unfolds when the tensile force exerted on it exceeds a predetermined sequence-specific threshold between 5 pN (four heptads) and 13 pN (eight heptads) (Fig. 1e, Fig. S1). As shown in Fig. 1e, the folded coiled-coils start to switch (or flicker at equilibrium) between folded and unfolded conformations when force reaches the threshold (Fig. 1e, state 1 and state 2, respectively), and become completely unfolded when force keeps increasing. The unfolding/refolding transitions are reversible in the relaxation rounds (Fig. 1e, black curves). We took this reversible transition feature as a main criterion to select sensors for further use in live measurements. The lower bound of the unfolding force threshold is set by the minimum number of heptads required to form a coiled-coil (3.5 heptads for most known anti-parallel coiled-coils)[32,33]. Higher force thresholds can be achieved by increasing the number of heptads but with diminishing returns the longer it is extended. The maximum number of heptads is also limited by the increasing likelihood of unfolding hysteresis when the number of heptads exceeds 6 (Fig. 1e, FEC# (6)), suggested by the additional folding intermediate (Fig.1e, state 2*). To detect forces smaller than 5 pN, we engineered the stalk region of mouse cytoplasmic dynein, an anti-parallel coiled-coil that unfolds at 3 pN (Fig. 1e, FEC # (1)). Our library of four coiled-coils (hereafter called cc-3pN, cc-5pN, cc-7pN, cc-10pN) is sufficient to cover the physiological range of most forces on a single molecule with ~2 pN resolution. Note that varying the pulling speed or the replacement of the linkers of similar lengths between the two α-helices has a minimal influence on the unfolding force threshold of the coiled-coil, consistent with previous models and measurements[34,35] (Fig. S2).

We developed two categories of readout modules: *recorders* and *live reporters*. Recorders use bipartite systems that are irreversible (or very slowly reversible), so that they keep emitting signal for a long time after the force-sensing module has unfolded, and therefore “records” (or “integrates”) the maximum force the sensor has experienced in the past (Fig. 1f). Here, we present three recorders: the split-Nanoluc, split-GFP, and TEV systems. The split-Nanoluc system is composed of a 11-aa (amino acid) peptide (HiBit) used as linker between the two α-helices, and the rest of the Nanoluc (LgBit) expressed in the cell[36,37]. When force opens the force-sensing element, a full Nanoluc is reconstituted and luminescence is produced following the addition of a Nanoluc substrate (e.g. furimazine). Similarly, the split-GFP system is composed of GFP11, a 16-aa peptide whose sequence corresponds to the 11$^{th}$ β-strand of the GFP, used as a linker between the α-helices of the force-sensing module, and GFP1-10, the GFP lacking the 11$^{th}$ β-strand (not fluorescent by itself), which is expressed in the cell. When force is low, no fluorescence is emitted. Upon opening of the force-sensing element, GFP11 is exposed and binds with GFP1-10, matures, and emits fluorescence[38]. Because the off-rate constant of the split-GFP system is very slow (~hours), fluorescence persists even after the force vanished[39]. The TEVp system uses a 7-aa TEV protease (TEVp) cleavage site as a linker, and the TEVp expressed in the cell, such that the force sensing element is cleaved after it is unfolded by force[40]. “Live reporters” are constituted of a peptide tag used as linker and a complementary peptide or domain fused to a fluorescent protein, which is expressed in the cell (Fig. 1f). Here, we present the reversible binder-tag systems

IAAL-E3/IAAL-K3, an artificial binding pair[41]. Under low force, fluorescence is diffuse, but when high force unfolds the force-sensing element, the fluorescent protein re-localizes to the force sensor. Because the tags used are reversible with a fast off rate constant, when force is released, the fluorescent protein detaches, and fluorescence becomes diffuse again[42].

We demonstrate the use of our new sensors by measuring the *in vivo* forces on key force-bearing cytoplasmic proteins. First, we measured 6 pN peak tension on formin Cdc12 (Fig. 2a) using the split-Nanoluc (Fig. 2b, Fig. S3) and split-GFP (Fig. 2c, Fig. S4) recorder readouts. Cdc12 polymerizes actin filaments and connects them to the plasma membrane during cytokinesis in the fission yeast *Schizosaccharomyces pombe*[43,44]. We also followed the temporal evolution of the force on Cdc12 using the live recorder readout IAAL-K3/ mEGFP-IAAL-E3 (Fig. 2d). Timelapse imaging indicates that force on Cdc12 starts to exceed 3 pN during the ring constriction phase and drops below 3 pN before the ring fully disassembles. Second, we measured the forces on epsin Ent1, an adaptor protein involved in clathrin-mediated endocytosis. Ent1 contains an actin cytoskeleton-binding (ACB) domain and a clathrin-binding motif (CBM)[45,46] (Fig. 2e). Using the split-Nanoluc readout, we detected a peak force of 6 pN before the ACB domain (Fig. 2f). Importantly, elimination of the C-terminal CBM decreased the force by 75%, indicating that substantial tension on Ent1 is mediated by its interaction directly with the clathrin lattice, and not just from the actin cytoskeleton, as previously thought (Fig. 2f, Fig. S5). In agreement with this result, dual-color TIRF imaging of the force on Ent1 and the F-actin crosslinking protein fimbrin, which is used as a fiduciary marker of filamentous actin at endocytic sites (Fig. 2g), indicates that force on Ent1 starts to accumulate ~30 seconds before F-actin starts assembling[47,48] (Fig. 2h, Fig. S5). This surprising result directly demonstrates for the first time that forces during endocytosis are not exclusively produced by actin assembly. Third, in *C. elegans*, we inserted the force sensors using the split-GFP recorder readout into β-spectrin (UNC-70), which forms rungs between periodic F-actin rings in the submembrane region of axons (termed membrane-associated periodic skeleton or MPS)[49,50] (Fig. 2i, Fig. S6). We measured a peak force of ~8 pN on β-spectrin, and found that dematin/UNC-115, a protein that is required for MPS organization, is needed to maintain the tension (Fig. 2j-k). This result suggests that the maximal force experienced by a single β-spectrin in freely-moving worms is higher than that measured in paralyzed worms, where FRET-based force sensors report an average force of 1.5 pN at the same location on β-spectrin[51]. Fourth, we measured the force in the linker of nucleoskeleton and cytoskeleton (LINC) complex responsible for force transmission across the nuclear envelope and nuclear positioning[52–54]. To this end, we inserted the mechano-sensor into mini-Nesprin-2G, a smaller functional version of the Nesprin-2G protein that associates with actin on the cytosolic side and the SUN protein within the lumen of the nuclear envelope (Fig 2l). Upon co-transfection with TEV protease, we observed a diagnostic cleavage product from mini-Nesprin-2G with cc-5 pN, while the mini-Nesprin-2G with cc-10 pN remained resistant to proteolytic cleavage. This observation is consistent with previous studies showing that mini-Nesprin-2G is under actin-dependent tension in the single pN range[55,56]. (Fig. 2d, Fig. S7). Finally, by using

the coiled-coil mechano-sensors with split-GFP recorder readout in the key focal adhesion protein vinculin (Fig 2n), we measured a maximum force on single vinculin above 10 pN (Fig. 2o-p, Fig. S8), higher than the 2 pN average from ensemble measurements with FRET-based force sensors[4,11,57]. This suggests that a small percentage of vinculin molecules mediate most of the tension between talin and F-actin[12,13].

In summary, we present here a new modular approach for *in vivo* force measurement using mechano-sensors that are genetically encoded, small, compatible with a versatile readout selection, and accessible to most labs. We expect the calibrated coiled-coils are compatible with a broader range of readouts not directly tested in this paper, including FRET-based readouts. The validity of our approach is independently demonstrated on different proteins and in multiple biological systems. We envision this plug-and-use architecture of mechano-sensors to herald an explosion of *in vivo* force measurements and to truly open the gate to quantitative mechanobiology.

## Material and Methods

### *Protein purification and biotinylation*

DNA sequences coding coiled-coils were synthesized from IDT and subcloned into BL21 (DE3) E. coli (New England BioLabs) for protein expression. Coiled-coils were expressed with GST fusion at the N-terminus and Avi-tag at the C-terminus. Cleared bacteria lysates were purified by binding to Glutathione Sepharose 4B beads (GE Healthcare). The GST tag was cleaved by PreScission Protease (Sigma-Aldrich) afterwards. Avi-tag in purified coiled-coil proteins was exchanged into biotinylation buffer (25 mM HEPES, 200 mM potassium glutamate, pH 7.7) and biotinylated with 50 mM bicine buffer, 50 µg/mL BirA, pH 8.3, 10 mM ATP, 10 mM magnesium acetate, and 50 µM d-biotin (Avidity) at 4°C overnight.

### *DNA handle preparation and crosslinking with protein*

The DNA handle used for protein attachment in single-molecule experiments was produced via PCR, yielding a 2,260 base pair fragment. This DNA fragment was modified to include a thiol group (-SH) at one end and two digoxigenin moieties at the other. For the crosslinking process, as described previously[60,61], DNA handle was conjugated first with DTDP at pH 5.5 and excess DTDP was removed by spin column. Then purified proteins were mixed with the DTDP-treated DNA handle at a molar ratio of 50:1 (protein to DNA). This mixture was prepared in a 100 mM phosphate buffer containing 500 mM NaCl at pH 8.5 and incubated overnight at room temperature.

### *Single-molecule manipulation experiments*

All single-molecule experiments were performed using dual-trap high-resolution optical tweezers[60,62,63]. In brief, the two optical traps were created by focusing two orthogonally polarized beams through a water-immersed 60× objective with a 1.2 numerical aperture (Olympus). These beams originated from a single 1,064-nm laser generated by a solid-state laser (Spectra-Physics) and were then split. One of the beams was deflected by a mirror mounted on a piezoelectrically controlled stage (Mad City Labs), which could tilt along two orthogonal axes, allowing for relative movement between the traps. The outgoing laser beams were collimated by a second water immersion objective, split, and projected onto two position-sensitive detectors (Pacific Silicon Sensor). Bead displacements were detected using back-focal plane interferometry. To prepare the DNA handle crosslinked proteins, they were incubated with anti-digoxigenin antibody-coated polystyrene beads (2.17 μm in diameter, Spherotech) for 15 minutes. This mixture was then diluted with 1 mL of phosphate-buffered saline (PBS) and introduced into the top channel of a microfluidic chamber. Meanwhile, streptavidin-coated beads (1.86 μm in diameter) were introduced into the bottom channel of the chamber. Both channels were connected to a central channel via capillary tubes, where the beads were trapped. Once a bead from each type was captured, a single protein was tethered between them by bringing the two beads close together. The tethered molecule underwent pulling and relaxation by adjusting the trap separation at a rate of 10 nm/s. The optical tweezers experiments were conducted in PBS at 23 (± 1) °C. The buffer in the central channel was supplemented with an oxygen scavenging system as described elsewhere. Data were processed using MATLAB codes, also described elsewhere[60,64], and unfolding forces were determined from the force-extension curves.

*Steered molecular dynamics (SMD) simulation*

Structures of coiled-coils were predicted from AlphaFold2[65]. We rotated the coiled-coil so that the vector from the N terminus to the C terminus aligned with the x-axis, ensuring a consistent initial condition for all coiled-coils. We used Qiwik to generate NAMD's configuration files. The total displacement was set to 200 Å with a margin of 15 Å for water molecules, and the salt concentration was set to 0.15mol/L. We anchored the first residue of the coiled coils and pulled the last one. The speed at which we pulled the SMD's dummy atom was 2.5e-5 A/fs (2500 m/s), and the spring constant was 1e-2kcal/mol/Å$^2$ (6.949e$^{-1}$ pN/ Å). This unrealistically high pulling speed was set up to obtain results within a reasonable time (~1 week per coiled-coil).

Before running the SMD simulation, we performed a minimization for 5,000 steps, followed by annealing by increasing the temperature from 60 K to 300 K. We increased the temperature by 1-degree increment and ran 600 steps between each increment. In total, it took 14,400 steps to increase the temperature to 300 K. Finally, we equilibrated the system by simulating it for 500,000 steps. We used the result of the equilibrated system as the initial condition of the SMD simulation. We used a step size of 2 fs for all the simulations mentioned.

To measure the force threshold, we measured the minimum force required to open the coiled coil in each iteration and then took the average over all forces. We used the Potential of Mean Force as described by Park and Schulten[66].

*Yeast strains and media*

The *S. pombe* strains in this paper are listed in Supplementary Table S1. The strains were created through CRISPR-mediated genome editing as outlined previously[67–69] and confirmed through sequencing of colony PCR products. Yeast cells were cultured in YE5S medium (Yeast Extract supplemented with 0.225 g/L each of uracil, adenine, lysine, histidine, and leucine) and imaged on gelatin pads made with EMM5S (Edinburgh Minimum media supplemented with 0.225 g/L each of uracil, adenine, lysine, histidine, and leucine). Before imaging, yeast cells were grown at 32 °C with continuous shaking at 200 rpm overnight, allowing them to reach the exponential growth phase with $OD_{595nm}$ values between 0.3 and 0.5.

*Confocal microscopy for yeast cells*

Live imaging of *S. pombe* cells was performed on a 25% gelatin pad at room temperature, using a Nikon TiE inverted microscope with a CSU-W1 Confocal Scanning Unit from Yokogawa Electric Corporation (Tokyo, Japan). The microscope was equipped with a CFI Plan Apo 100X/1.45NA Phase objective from Nikon. Image acquisition was performed using an iXon Ultra888 EMCCD camera from Andor (Belfast, UK). For imaging GFP, an excitation wavelength of 488nm from an argon-ion laser was used, and the fluorescence emission was filtered via a single band pass filter 510/25 in the Spectra X system. mCherry and sfCherry2 were excited from a 561nm argon-ion laser, and the fluorescence emission was filtered through a single band pass filter 575/25 in the Spectra X system. To image the entire yeast cell, 21 optical slices were collected with a thickness of 0.5 µm, followed by maximum intensity projection to generate 2D images. For image display and analysis, the Fiji distribution of ImageJ provided by the National Institutes of Health (NIH, USA) was used[70]. *S. pombe* cells were also imaged on gelatin pads on BC43 CF tabletop confocal (Andor) with 100x Plan Apochromat oil immersion objective and preset excitation/emission combinations for GFP, mCherry and sfCherry.

*Measurement of bioluminescence*

Yeast cells were grown into the exponential phase in YE5S medium, pelleted, and resuspended in EMM5S to a final density of 1 $OD_{595nm}$/µL. 150 µL cells were mixed with 15 µL diluted substrate (Nano-Glo Live, Promega, 1:50 dilution.) and loaded into a black 96 well plate (Greiner Bio-One) before putting on a plate reader (BioTek synergy H1,

Agilent) for measurement. Luminescence signals were recorded 5 minutes after mixing cells with the substrate and normalized to the $OD_{595nm}$ of each well. Measurements were kept in a linear range predetermined as in Fig. S3.

*Nematode Strains and Maintenance*

Nematodes were cultured at 20°C on nematode growth medium plates that were seeded with OP50 bacteria.

*Nematode Microscopy and Data Analysis*

Detailed animal preparation for microscopy was published previously[71]. In brief, animals at their larval stage L4 were mounted on 10% agarose patch and paralyzed in a droplet of 10 mM Levamisole diluted in M9 medium. Images were acquired with a DMi8 inverted microscope (Leica) that is equipped with a VT-iSIM system (Biovision) and an ORCA-Flash 4.0 camera (Hamamatsu). The microscope was controlled by the MetaMorph Advanced Confocal Acquisition Software. Images were acquired with an HC PL APO 40x/1.30NA OIL CS2 objective at a 488nm laser line. Raw images were processed and analyzed in Fiji/ImageJ v2.3.0/1.53f51[70,72]. Images were acquired in single layers and then stacked into maximum projections. To capture the intensity signal along the entire length of PLM, which could not be acquired in a single field of view, multiple images along the length of the neurite were taken and stitched into a single image using the pairwise-stitching plugin with a linear blending fusion method[73]. To determine the mean fluorescence along the PLM neurite, a 5 pxl thick line was drawn along the center of the neurite and a signal intensity profile was generated by using the plot profile function and the signal intensity was averaged. To subtract background flourescence, the same signal intensity profile was acquired by shifting the drawn line from the center of the neurite by a few pxl into the non-neuronal tissue directly contacting the neurite. The signal intensity was calculated in arbitrary units as $I_{mean}=I_{mean}$ (neurite)- $I_{mean}$ (background).

*Plasmids and transient transfections for TEVp expressing cells*

The TEV module was cloned using standard cloning techniques into the nesprin TSmod 25 in pcDNA3.1 (https://www.addgene.org/browse/sequence/244038/)[74]. The mCerulean and mVenus sequences were removed and replaced with either the 5 pN or 10 pN sensor leading to an insertion between the N-terminal actin-binding CH domain (1-485) and the C-terminal KASH SUN-binding domain (6525–6874) (Fig. 2I)

U2OS cells were cultured on coverslips and transfected using Lipofectamine 3000 reagent (ThermoFisher) according to the manufacturer's instructions. Immunoblot protocols were executed as previously described[75]. Briefly, 10 µg of protein were resolved by 10% SDS–PAGE gels and transferred onto polyvinylidene fluoride membranes (Bio-Rad). Membranes were blocked in 4% (wt/vol) milk in PBS + 0.1% (vol/vol) Tween-20 (Sigma-Aldrich). Primary and horseradish peroxidase-conjugated secondary antibodies

were diluted in blocking buffer. A ChemiDoc gel imaging system (Bio-Rad) was used to visualize chemiluminescence.

For immunofluorescence, cells were fixed with 4% PFA/PBS for 15 min, permeabilized with 0.3% Triton X-100/PBS for 3 min, and blocked with 4% BSA/PBS (Sigma-Aldrich) for 1 hour. Coverslips were incubated for one hour with primary antibodies: FLAG (Millipore Sigma F3165, 1:500), HA (Roche 11867423001, 1:500), or LaminA (Invitrogen MA1-06101, 1:500). Samples were washed 2x with PBS for 5 min, incubated with Alexa Fluor (Life Technologies) secondary antibodies for one hour, and then washed 3x with PBS and mounted with ProLong Gold Antifade reagent + DAPI (Thermo Fisher P36935). Images were acquired on an LSM 880 laser scanning confocal microscope (Zeiss) with Airyscan using a C Plan-Apochromat 63×/1.40 oil DIC M27 objective using ZEN 2.1 software (Zeiss).

*Statistical evaluation*

Statistical evaluation was performed with GraphPad Prism (version 7). The dataset was first tested for normality distribution by using the D´Agostino and Pearson test to judge the use of non- vs parametric statistical tests. For formin Cdc12 and Vinculin force measurements, one-way ANOVA with Tukey's multiple comparison tests was used with MATLAB (MathWorks, version 2021).

## Acknowledgement

We thank the Yale West Campus Imaging Core for providing resources for microscopy and Keck DNA Sequencing Facility at Yale for their assistance. We thank Dr. Chengye Feng for helping to make the *C. elegans* strains with split-GFP readouts. The unc-115(ky275) strain was provided by the Caenorhabditis Genetic Center (CGC), which is funded by NIH Office of Research Infrastructure Programs (P40 OD010440). OG is supported by a Walter-Benjamin Scholarship funded by the Deutsche Forschungsgemeinschaft (DFG, German Research Foundation) Project# 465611822. SY is supported by the NIH grant R35GM131744. YZ is supported by the NIH grant R35GM131714. JB is supported by the NIH grants R21GM132661, R01GM115636 and the grant SA-CMC-2021-037 from the Research Corporation for Scientific Advancement.

## Declaration of interests

Julien Berro, Yuan Ren and Yongli Zhang have a pending patent application PCT/US2023/069505.

## Figures

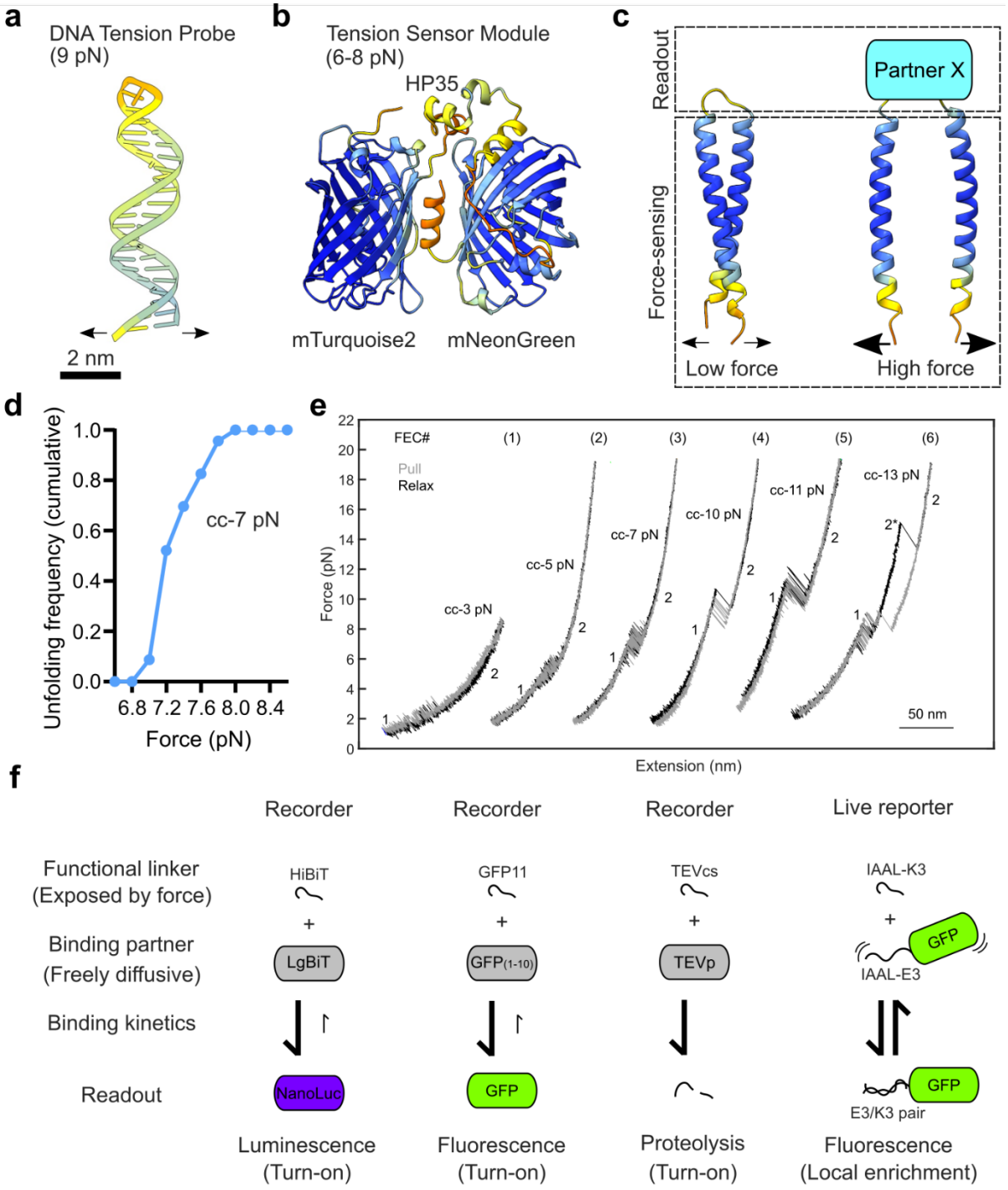

Figure 1. **Rational design and calibration of coiled-coils as force-sensing modules.** **a**, A DNA hairpin (TP9) with defined nucleotide composition unfolds at a characteristic force threshold[2]. Fluorescence readouts (such as a fluorophore-quencher pair) by chemical modifications on the DNA hairpin correlate force with fluorescence. **b**, An elastic peptide (HP35) sandwiched by two fluorescent proteins (mTurquoise2 and mNeonGreen) form a genetically encoded force sensor[16,58]. The FRET efficiency between the two fluorescent proteins depends strongly on the peptide length, which scales linearly with force magnitude within a small range. **c**, Calibrated coiled-coils can be used as the force-sensing module to correlate mechanical force to their conformational change. Readouts are specific protein binding to the linkers of mechanically unfolded coiled-coils. Molecules in **a**-**c** are shown at the same scale, and the structures are predicted by AlphaFold3[59] and colored with b-factor palette. Arrows indicate the force pulling directions. **d**, Cumulative unfolding probability of the coiled-coil force sensor cc-7 pN as a function of force. The jump of the unfolding probability from below 0.1 to above 0.9 within 1 pN indicates a near-digital response to mechanical forces. **e**, Representative force-extension curves (FECs) obtained by pulling (grey) or relaxing (black) coiled-coil sensors using optical tweezers. The conformations of the coiled coils are labeled: 1, folded state; 2, unfolded state; and 2*, partially unfolded state. **f**, The selection of functional linkers and their binding partners offers great freedom in choosing force sensor readouts. Broadly, readouts with slow unbinding kinetics are force recorders (HiBiT and LgBiT; GFP11 and GFP1-10; TEV cleaving site (TEVcs) and TEVp), while readouts with fast unbinding kinetics are force live reporters (IAAL-K3 and IAAL-E3).

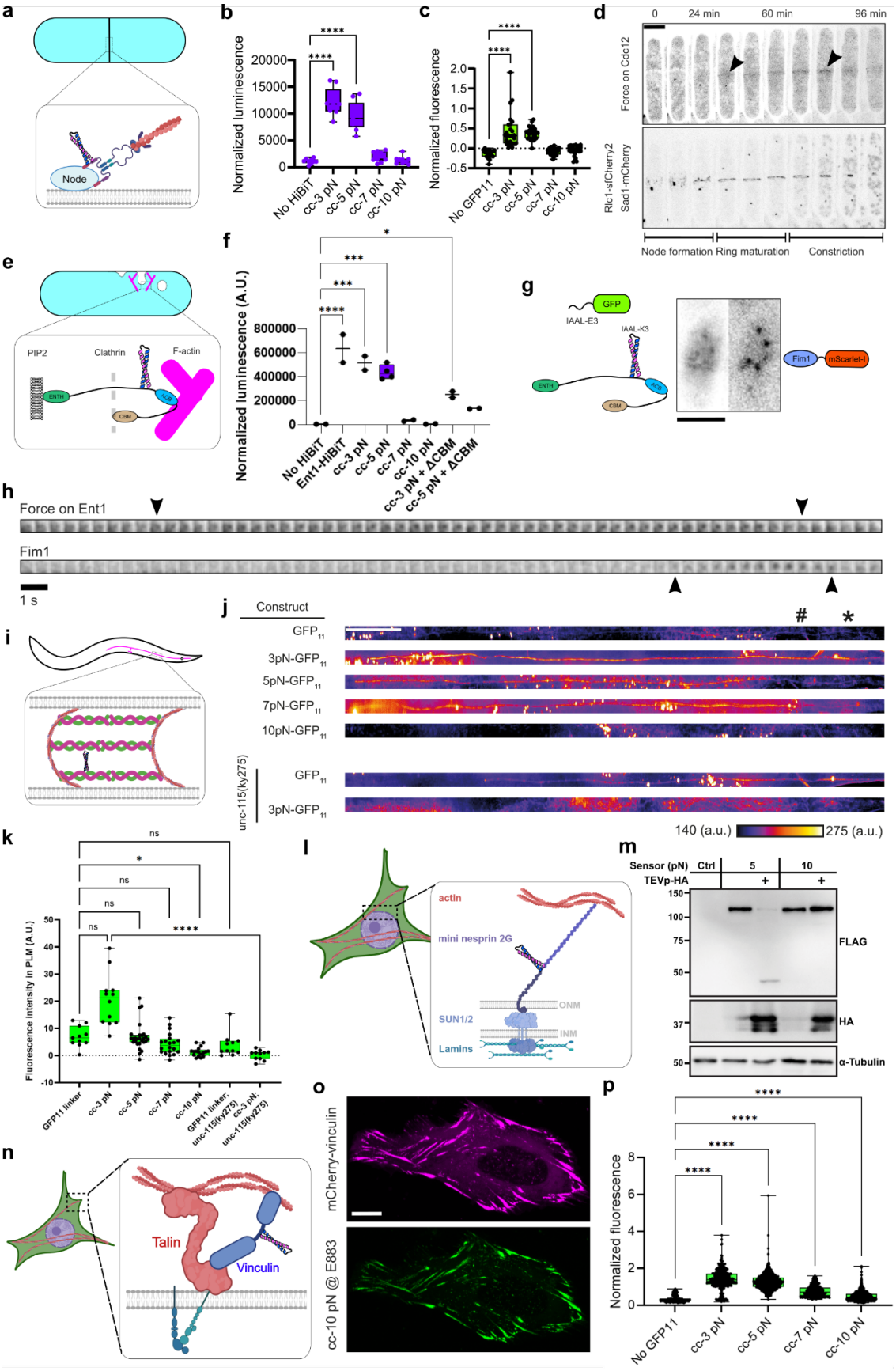

**Figure 2. Modular assembly of mechano-sensors with versatile readouts in multiple biological systems. a**, Schematic of the role of Cdc12 during cytokinesis in the fission yeast *S. pombe*. Cdc12 nucleates F-actin assembly and bridges F-actin to the cytokinetic nodes on the plasma membrane. Force sensors are inserted after A216 at cdc12 genomic location. **b**, Force measurement on Cdc12 via the splitNanoLuc approach. Comparisons are ordinary one-way ANOVA with Tukey's multiple comparison tests with "No-HiBiT" as the control and only displayed for pairs where p values is less than 0.05. ****, p<0.0001. **c**, Force measurement on Cdc12 via the splitGFP approach. Comparisons are ordinary one-way ANOVA with Tukey's multiple comparison tests with "No-GFP11" as the control and only displayed for pairs where p values is smaller than 0.05. ****, p<0.0001. **d**, Timelapse of force on Cdc12 (cc-3 pN with IAAL-K3 linker and mEGFP-IAAL-E3 binder) and the cytokinetic ring (Rlc1-sfCherry) during fission yeast cytokinesis. Sad1-mCherry is used to locate the dividing spindle pole body and to time cytokinesis. Force on Cdc12 starts to build up above 3 pN at the beginning of ring maturation and drops below 3 pN before the ring fully disassembles. Arrowheads indicate the recruitment of mEGFP to Cdc12 when cc-3 pN is unfolded by force. Scale bar, 5 μm. **e**, Schematic of Ent1 and its interacting partners during clathrin-mediated endocytosis (CME) in the fission yeast. Force sensors are inserted after P571 at ent1 genomic location. ENTH, N-terminal lipid-binding domain. ACB, actin cytoskeleton-binding domain. CBM, clathrin-binding motif. **f**, Force measurement on Ent1 via the splitNanoLuc approach. ~6 pN force is detected on Ent1 and the deletion of CMB decreased but did not diminish the force on Ent1. Comparisons are ordinary one-way ANOVA with "No-HiBiT" as the control and only displayed for pairs where p values is smaller than 0.05. *, p<0.05; **, p<0.01; ***, p<0.001; ****, p<0.0001. **g**, Dual-color TIRF is used to simultaneously track the force on Ent1 (cc-3 pN with IAAL-K3 linker and mEGFP-IAAL-E3 binder) and the F-actin dynamics (Fim1-mScarlet-I) in fission yeast cells. Scale bar, 5 μm. **h**, Montage of a representative CME event. Note that force on Ent1 increases to above 3 pN ~30 s before F-actin assembly. Arrowheads denote the first and last frames where force on Ent1 is above 3 pN. **i**, Position of the sensory PLM neuron in the nematode *C. elegans*. Spectrins (UNC-70 and SPC-1), shown as spirals in the zoomed region, form the central building block of the membrane associated periodic skeleton (MPS), which consists of actin rings that are interspaced by spectrin tetramers below the plasma membrane throughout the entire length of the axon. Force sensors were inserted into the genomic unc-70 locus between spectrin repeats 8 and 9 (after R1167). Only one coiled-coil is shown for clarity. See Fig. S6 for details of force sensor insertion. **j**, Representative maximum projections of *C. elegans* strains expressing UNC-70 with force sensors together with GFP1-10 under a PLM specific promoter (mec-17p) in wildtype or unc-115(ky275) mutant. Signal intensity is color coded according to the displayed color bar. Scale bar, 50 μm. The position of the cell body (*) and the rectum (#) are indicated. Background fluorescence outside of the axon region was not included in quantification. Example images are rescaled in X and Y dimension (1:2) to enlarge the neurite diameter for better visualization. **k**, Quantification of fluorescence in **j**. Multiple comparisons with Kruskal-Wallis test. *, p<0.05. ****, p<0.0001. **l**, Mini-Nesprin-2G transmits forces from cytoplasmic F-actin to SUN in the nucleus. cc-

5pN or cc-10 pN with TEV protease (TEVp) recognition motifs were inserted between the N-terminal actin-binding CH domain (1-485) and the C-terminal KASH SUN-binding domain (6525–6874) **m**, Immunoblot of cell lysates obtained from U2OS cells transfected with the indicated 5 pN or 10 pN TEVp-readout sensors in mini-Nesprin-2G. Note that cleavage of the 5 pN sensor is observed upon co-transfection with TEVp, whereas the 10 pN sensor version is resistant to TEVp activity (TEVp-HA +). Representative of two independent repeats. **n**, Vinculin binds to talin and F-actin in focal adhesions and contributes to force transmission between the extracellular matrix and the cytoskeleton. **o**, U2OS cells expressing fluorescently tagged vinculin (mCherry-vinculin) and cc-10 pN with the split-GFP readout inserted after E883. GFP signals at focal adhesions indicate that peak force on vinculin exceeds 10 pN. Scale bar, 10 μm. See also Fig. S8. **p**, Quantification of force on vinculin. Data pooled from two independent experiments. Comparisons are ordinary one-way ANOVA with Tukey's multiple comparison tests with "No-GFP11" as the control. ****, $p<0.0001$. All schematics in this figure are for illustrative purpose only and not drawn to scale. Some schematics are created with BioRender.com.

## References

1. Wang, X. & Ha, T. Defining single molecular forces required to activate integrin and notch signaling. *Science* **340**, 991–994 (2013).
2. Blakely, B. L. *et al.* A DNA-based molecular probe for optically reporting cellular traction forces. *Nat Methods* **11**, 1229–1232 (2014).
3. Zhang, Y., Ge, C., Zhu, C. & Salaita, K. DNA-based digital tension probes reveal integrin forces during early cell adhesion. *Nat Commun* **5**, 5167 (2014).
4. Grashoff, C. *et al.* Measuring mechanical tension across vinculin reveals regulation of focal adhesion dynamics. *Nature* **466**, 263 (2010).
5. Suzuki, A. *et al.* How the kinetochore couples microtubule force and centromere stretch to move chromosomes. *Nat Cell Biol* **18**, 382–392 (2016).
6. Amiri, S. *et al.* Intracellular tension sensor reveals mechanical anisotropy of the actin cytoskeleton. *Nat Commun* **14**, 8011 (2023).
7. Polacheck, W. J. & Chen, C. S. Measuring cell-generated forces: a guide to the available tools. *Nat Methods* **13**, 415–423 (2016).
8. Jurchenko, C. & Salaita, K. S. Lighting Up the Force: Investigating Mechanisms of Mechanotransduction Using Fluorescent Tension Probes. *Mol Cell Biol* **35**, 2570–2582 (2015).
9. LaCroix, A. S., Rothenberg, K. E., Berginski, M. E., Urs, A. N. & Hoffman, B. D. Chapter 10 - Construction, imaging, and analysis of FRET-based tension sensors in living cells. in *Methods in Cell Biology* (ed. Paluch, E. K.) vol. 125 161–186 (Academic Press, 2015).
10. Ham, T. R., Collins, K. L. & Hoffman, B. D. Molecular Tension Sensors: Moving Beyond Force. *Curr Opin Biomed Eng* **12**, 83–94 (2019).

11. LaCroix, A. S., Lynch, A. D., Berginski, M. E. & Hoffman, B. D. Tunable molecular tension sensors reveal extension-based control of vinculin loading. *eLife* **7**, e33927 (2018).
12. Ringer, P. *et al.* Multiplexing molecular tension sensors reveals piconewton force gradient across talin-1. *Nature Methods* **14**, 1090–1096 (2017).
13. Lemke, S. B., Weidemann, T., Cost, A.-L., Grashoff, C. & Schnorrer, F. A small proportion of Talin molecules transmit forces at developing muscle attachments in vivo. *PLoS Biol* **17**, e3000057 (2019).
14. Jo, M. H. *et al.* Determination of single-molecule loading rate during mechanotransduction in cell adhesion. *Science* **383**, 1374–1379 (2024).
15. Hu, Y. *et al.* DNA-based ForceChrono probes for deciphering single-molecule force dynamics in living cells. *Cell* **0**, (2024).
16. Abella, M., Andruck, L., Malengo, G. & Skruzny, M. Actin-generated force applied during endocytosis measured by Sla2-based FRET tension sensors. *Developmental Cell* **56**, 2419-2426.e4 (2021).
17. Liu, J. *et al.* Tension Gauge Tethers as Tension Threshold and Duration Sensors. *ACS Sens.* **8**, 704–711 (2023).
18. Mosayebi, M., Louis, A. A., Doye, J. P. K. & Ouldridge, T. E. Force-Induced Rupture of a DNA Duplex: From Fundamentals to Force Sensors. *ACS Nano* **9**, 11993–12003 (2015).
19. Cocco, S., Monasson, R. & Marko, J. F. Force and kinetic barriers to unzipping of the DNA double helix. *Proceedings of the National Academy of Sciences* **98**, 8608–8613 (2001).

20. Sun, X., Hao, P. & Wu, N. DNA-Based Mechanical Sensors for Cell Applications. *Chemistry* **5**, 1546–1559 (2023).
21. Liu, Y. *et al.* DNA-based nanoparticle tension sensors reveal that T-cell receptors transmit defined pN forces to their antigens for enhanced fidelity. *Proceedings of the National Academy of Sciences* **113**, 5610–5615 (2016).
22. Eder, D., Basler, K. & reports, A.-C. Challenging FRET-based E-Cadherin force measurements in Drosophila. *Scientific reports* (2017).
23. Cost, A.-L., Ringer, P., Anna, C.-G. & Grashoff, C. How to measure molecular forces in cells: a guide to evaluating genetically-encoded FRET-based tension sensors. **8**, 96–105 (2015).
24. As, L., Ke, R., Me, B., An, U. & Bd, H. Construction, imaging, and analysis of FRET-based tension sensors in living cells. *Methods in cell biology* **125**, (2015).
25. Aird, E. J., Tompkins, K. J., Ramirez, M. P. & Gordon, W. R. Enhanced Molecular Tension Sensor Based on Bioluminescence Resonance Energy Transfer (BRET). *ACS Sens.* **5**, 34–39 (2020).
26. Ren, Y. *et al.* Force redistribution in clathrin-mediated endocytosis revealed by coiled-coil force sensors. *Sci Adv* **9**, eadi1535 (2023).
27. Ren, Y., Yang, J., Jin, H., Zhang, Y. & Berro, J. *Force Redistribution in Clathrin-Mediated Endocytosis Revealed by Phase-Separating Force Sensors*. 2021.06.29.450294 https://www.biorxiv.org/content/10.1101/2021.06.29.450294v3 (2021) doi:10.1101/2021.06.29.450294.
28. BERRO, J., Ren, Y. & Zhang, Y. Coiled-coil peptides for force-dependent applications. (2024).

29. McClain, D. L., Woods, H. L. & Oakley, M. G. Design and Characterization of a Heterodimeric Coiled Coil that Forms Exclusively with an Antiparallel Relative Helix Orientation. *J. Am. Chem. Soc.* **123**, 3151–3152 (2001).
30. Park, W. M. Coiled-Coils: The Molecular Zippers that Self-Assemble Protein Nanostructures. *Int J Mol Sci* **21**, 3584 (2020).
31. Truebestein, L. & Leonard, T. A. Coiled-coils: The long and short of it. *Bioessays* **38**, 903–916 (2016).
32. Su, J. Y., Hodges, R. S. & Kay, C. M. Effect of Chain Length on the Formation and Stability of Synthetic .alpha.-Helical Coiled Coils. *Biochemistry* **33**, 15501–15510 (1994).
33. Litowski, J. r. & Hodges, R. s. Designing heterodimeric two-stranded α-helical coiled-coils: the effect of chain length on protein folding, stability and specificity. *The Journal of Peptide Research* **58**, 477–492 (2001).
34. Carrion-Vazquez, M. *et al.* Mechanical and chemical unfolding of a single protein: A comparison. *Proc. Natl. Acad. Sci. U.S.A.* **96**, 3694–3699 (1999).
35. Evans, E. Probing the Relation Between Force—Lifetime—and Chemistry in Single Molecular Bonds. *Annual Review of Biophysics* **30**, 105–128 (2001).
36. Biewenga, L., Rosier, B. J. H. M. & Merkx, M. Engineering with NanoLuc: a playground for the development of bioluminescent protein switches and sensors. *Biochemical Society Transactions* **48**, 2643–2655 (2020).
37. Schwinn, M. K. *et al.* CRISPR-Mediated Tagging of Endogenous Proteins with a Luminescent Peptide. *ACS Chem. Biol.* **13**, 467–474 (2018).

38. Kamiyama, D. *et al.* Versatile protein tagging in cells with split fluorescent protein. *Nature Communications* **7**, 11046 (2016).

39. Romei, M. G. & Boxer, S. G. Split Green Fluorescent Proteins: Scope, Limitations, and Outlook. *Annu Rev Biophys* **48**, 19–44 (2019).

40. Raran-Kurussi, S., Cherry, S., Zhang, D. & Waugh, D. S. Removal of Affinity Tags with TEV Protease. *Methods Mol Biol* **1586**, 221–230 (2017).

41. Lindhout, D. A., Litowski, J. R., Mercier, P., Hodges, R. S. & Sykes, B. D. NMR solution structure of a highly stable de novo heterodimeric coiled-coil. *Biopolymers* **75**, 367–375 (2004).

42. Liu, B. *et al.* Biosensors based on peptide exposure show single molecule conformations in live cells. *Cell* **184**, 5670-5685.e23 (2021).

43. Shekhar, S. *et al.* Formin and capping protein together embrace the actin filament in a ménage à trois. *Nature Communications* **6**, 8730 (2015).

44. Coffman, V. C., Sees, J. A., Kovar, D. R. & Wu, J.-Q. The formins Cdc12 and For3 cooperate during contractile ring assembly in cytokinesis. *J Cell Biol* **203**, 101–114 (2013).

45. Aguilar, R. C., Watson, H. A. & Wendland, B. The Yeast Epsin Ent1 Is Recruited to Membranes through Multiple Independent Interactions. *J. Biol. Chem.* **278**, 10737–10743 (2003).

46. Skruzny, M. *et al.* Molecular basis for coupling the plasma membrane to the actin cytoskeleton during clathrin-mediated endocytosis. *Proc Natl Acad Sci U S A* **109**, E2533–E2542 (2012).

47. Berro, J. & Pollard, T. D. Local and global analysis of endocytic patch dynamics in fission yeast using a new 'temporal superresolution' realignment method. *Mol Biol Cell* **25**, 3501–3514 (2014).
48. Lemière, J., Ren, Y. & Berro, J. Rapid adaptation of endocytosis, exocytosis, and eisosomes after an acute increase in membrane tension in yeast cells. *eLife* **10**, e62084 (2021).
49. Unsain, N., Stefani, F. D. & Cáceres, A. The Actin/Spectrin Membrane-Associated Periodic Skeleton in Neurons. *Front. Synaptic Neurosci.* **10**, (2018).
50. Costa, A. R. *et al.* The membrane periodic skeleton is an actomyosin network that regulates axonal diameter and conduction. *eLife* **9**, e55471 (2020).
51. Krieg, M., Dunn, A. R. & Goodman, M. B. Mechanical Control of the Sense of Touch by β Spectrin. *Nat Cell Biol* **16**, 224–233 (2014).
52. Crisp, M. *et al.* Coupling of the nucleus and cytoplasm: role of the LINC complex. *J Cell Biol* **172**, 41–53 (2006).
53. Gottardi, C. J. & Luxton, G. W. G. Nesprin-2G tension fine-tunes Wnt/β-catenin signaling. *J Cell Biol* **219**, e202009042 (2020).
54. Srivastava, L. K. & Ehrlicher, A. J. Sensing the squeeze: nuclear mechanotransduction in health and disease. *Nucleus* **15**, 2374854 (2024).
55. Arsenovic, P. T. *et al.* Nesprin-2G, a Component of the Nuclear LINC Complex, Is Subject to Myosin-Dependent Tension. *Biophys J* **110**, 34–43 (2016).
56. Carley, E. *et al.* The LINC complex transmits integrin-dependent tension to the nuclear lamina and represses epidermal differentiation. *eLife* **10**, e58541 (2021).

57. Rothenberg, K. E., Scott, D. W., Christoforou, N. & Hoffman, B. D. Vinculin Force-Sensitive Dynamics at Focal Adhesions Enable Effective Directed Cell Migration. *Biophys J* **114**, 1680–1694 (2018).

58. Austen, K. *et al.* Extracellular rigidity sensing by talin isoform-specific mechanical linkages. *Nature Cell Biology* **17**, 1597–1606 (2015).

59. Abramson, J. *et al.* Accurate structure prediction of biomolecular interactions with AlphaFold 3. *Nature* **630**, 493–500 (2024).

60. Gao, Y. *et al.* Single reconstituted neuronal SNARE complexes zipper in three distinct stages. *Science* **337**, 1340–1343 (2012).

61. Cecconi, C., Shank, E. A., Dahlquist, F. W., Marqusee, S. & Bustamante, C. Protein-DNA chimeras for single molecule mechanical folding studies with the optical tweezers. *Eur Biophys J* **37**, 729–738 (2008).

62. Yang, J., Jin, H., Liu, Y., Guo, Y. & Zhang, Y. A dynamic template complex mediates Munc18-chaperoned SNARE assembly. *Proceedings of the National Academy of Sciences* **119**, e2215124119 (2022).

63. Gao, Y., Sirinakis, G. & Zhang, Y. Highly Anisotropic Stability and Folding Kinetics of a Single Coiled Coil Protein under Mechanical Tension. *J. Am. Chem. Soc.* **133**, 12749–12757 (2011).

64. Jiao, J., Rebane, A. A., Ma, L. & Zhang, Y. Single-Molecule Protein Folding Experiments Using High-Precision Optical Tweezers. *Methods Mol Biol* **1486**, 357–390 (2017).

65. Jumper, J. *et al.* Highly accurate protein structure prediction with AlphaFold. *Nature* **596**, 583–589 (2021).

66. Goktas, M. *et al.* Molecular mechanics of coiled coils loaded in the shear geometry †Electronic supplementary information (ESI) available: CD measurements for the determination of secondary structure and the thermal stability of the coiled coils as well as additional results of the SMFS experiments and the SMD simulations are included in the supporting information. See DOI: 10.1039/c8sc01037d. *Chem Sci* **9**, 4610–4621 (2018).
67. Fernandez, R. & Berro, J. Use of a fluoride channel as a new selection marker for fission yeast plasmids and application to fast genome editing with CRISPR/Cas9. *Yeast* **33**, 549–557 (2016).
68. Fernandez, R. & Berro, J. CRISPR-Cas9 editing efficiency in fission yeast is not limited by homology search and is improved by combining gap-repair with fluoride selection. 2024.03.01.582946 Preprint at https://doi.org/10.1101/2024.03.01.582946 (2024).
69. Wood, V. *et al.* PomBase: a comprehensive online resource for fission yeast. *Nucleic Acids Research* **40**, D695–D699 (2012).
70. Schindelin, J. *et al.* Fiji: an open-source platform for biological-image analysis. *Nat Methods* **9**, 676–682 (2012).
71. Glomb, O., Lyu, M. & Yogev, S. Optimizing Visualization of Axonal Transport of Endogenous Cargo by Fluorescence Microscopy in Living Caenorhabditis elegans. *J Vis Exp* (2024) doi:10.3791/66236.
72. Schneider, C. A., Rasband, W. S. & Eliceiri, K. W. NIH Image to ImageJ: 25 years of image analysis. *Nat Methods* **9**, 671–675 (2012).

73. Preibisch, S., Saalfeld, S. & Tomancak, P. Globally optimal stitching of tiled 3D microscopic image acquisitions. *Bioinformatics* **25**, 1463–1465 (2009).

74. Östlund, C. *et al.* Dynamics and molecular interactions of linker of nucleoskeleton and cytoskeleton (LINC) complex proteins. *Journal of Cell Science* **122**, 4099–4108 (2009).

75. Tsai, P.-L. *et al.* Dynamic quality control machinery that operates across compartmental borders mediates the degradation of mammalian nuclear membrane proteins. *Cell Reports* **41**, 111675 (2022).

# Supplementary tables

**Supplementary Table S1**

*S. pombe* strains used in this study.

| Strain | Genotype | Used in | Reference |
|---|---|---|---|
| SpJB501 | *ent1-mEGFP fex1Δ fex2Δ ade6-M216 his3-D1 leu1-32 ura4-D18 h-* | Fig. S4, S5 | Berro lab collection |
| SpJB827 | *pil1Δ::GFP1-10 fex1Δ fex2Δ ade6-M216 his3-D1 leu1-32 ura4-D18 h-* | Fig. S5 | Berro lab collection |
| SpJB832 | *ent1-GSLIDL697AAAAAA-ent1-mEGFP fex1Δ fex2Δ ade6-M216 his3-D1 leu1-32 ura4-D18 h-* | Fig. S4 | Berro lab collection |
| SpJB944 | *pil1Δ::GFP1-10 ent1-P571-GFP11-ent1 fex1Δ fex2Δ ade6-M216 his3-D1 leu1-32 ura4-D18 h-* | Fig. S4 | Berro lab collection |
| SpJB963 | *pil1Δ::GFP1-10 cdc12-mScarlet-I fex1Δ fex2Δ ade6-M216 his3-D1 leu1-32 ura4-D18 h-* | Fig. 2c | Berro lab collection |
| SpJB1030 | *pil1Δ::mEGFP-IAAL-E3 fex1Δ fex2Δ ade6-M216 his3-D1 leu1-32 ura4-D18 h-* | Fig. S5 | Berro lab collection |
| SpJB1031 | *pil1Δ::mEGFP-IAAL-E3 ent1-P571-Dynein stalk-IAAL-K3-linker-ent1 fex1Δ fex2Δ ade6-M216 his3-D1 leu1-32 ura4-D18 h-* | Fig. S5 | Berro lab collection |
| SpJB1054 | *pil1Δ::mEGFP-IAAL-E3 ent1-P571-Dynein stalk-IAAL-K3-linker-ent1-GSLIDL697AAAAAA fex1Δ fex2Δ ade6-M216 his3-D1 leu1-32 ura4-D18 h-* | Fig. S5 | Berro lab collection |
| SpJB1173 | *pil1Δ::LgBiT fex1Δ fex2Δ ade6-M216 his3-D1 leu1-32 ura4-D18 h-* | Fig. 2f | Berro lab collection |
| SpJB1174 | *pil1Δ::LgBiT ent1-P571-Dynein stalk-2G-HiBiT-2G-linker-ent1, fex1Δ fex2Δ ade6-M216 his3-D1 leu1-32 ura4-D18 h-* | Fig. 2f, S3 | Berro lab collection |
| SpJB1192 | *pil1Δ::LgBiT ent1-P571-Oakley-p1-OnePlus-2G-HiBiT-2G-linker-ent1, fex1Δ fex2Δ ade6-M216 his3-D1 leu1-32 ura4-D18 h-* | Fig. 2f | Berro lab collection |
| SpJB1193 | *pil1Δ::LgBiT ent1-P571-Dynein stalk-2G-HiBiT-2G-linker-ent1-GSLIDL69AAAAAA, fex1Δ fex2Δ ade6-M216 his3-D1 leu1-32 ura4-D18 h-* | Fig. 2f | Berro lab collection |
| SpJB1194 | *pil1Δ::LgBiT ent1-HiBiT, fex1Δ fex2Δ ade6-M216 his3-D1 leu1-32 ura4-D18 h-* | Fig. S3 | Berro lab collection |
| SpJB1218 | *cdc12-A216-DyneinStalk-GFP11-cdc12-mScarlet-I pil1Δ::GFP1-10 fex1Δ fex2Δ ade6-M216 his3-D1 leu1-32 ura4-D18 h-* | Fig. 2c, S4 | Berro lab collection |
| SpJB1219 | *cdc12-A216-Oakley-p1-LV-L3S-GFP11-cdc12-mScarlet-I pil1Δ::GFP1-10 fex1Δ fex2Δ ade6-M216 his3-D1 leu1-32 ura4-D18 h-* | Fig. 2c, S4 | Berro lab collection |
| SpJB1229 | *cdc12-A216-Oakley-p1-GFP11-cdc12-mScarlet-I pil1Δ::GFP1-10 fex1Δ fex2Δ ade6-M216 his3-D1 leu1-32 ura4-D18 h-* | Fig. 2c, S4 | Berro lab collection |

| | | | |
|---|---|---|---|
| SpJB1230 | *cdc12-A216-Oakley-p1-OnePlus-GFP11-cdc12-mScarlet-I pil1Δ::GFP1-10 fex1Δ fex2Δ ade6-M216 his3-D1 leu1-32 ura4-D18 h-* | Fig. 2c, S4 | Berro lab collection |
| SpJB1287 | *fim1-mScarlet-I pil1Δ::mEGFP-IAAL-E3 ent1-P571-Dynein stalk-IAAL-K3-linker-ent1 fex1Δ fex2Δ ade6-M216 his3-D1 leu1-32 ura4-D18 h-* | Fig. 2g-h | Berro lab collection |
| SpJB1301 | *cdc12-A216-Oakley-p1-LV-L3S-2G-HiBiT-2G-linker-cdc12 pil1Δ::LgBiT fex1Δ fex2Δ ade6-M216 his3-D1 leu1-32 ura4-D18 h-* | Fig. 2b | Berro lab collection |
| SpJB1310 | *cdc12-A216-DyneinStalk-2G-HiBiT-2G-linker-cdc12 pil1Δ::LgBiT fex1Δ fex2Δ ade6-M216 his3-D1 leu1-32 ura4-D18 h-* | Fig. 2b | Berro lab collection |
| SpJB1311 | *cdc12-A216-Oakley-p1-2G-HiBiT-2G-linker-cdc12 pil1Δ::LgBiT fex1Δ fex2Δ ade6-M216 his3-D1 leu1-32 ura4-D18 h-* | Fig. 2b | Berro lab collection |
| SpJB1312 | *cdc12-A216-Oakley-p1-OnePlus-2G-HiBiT-2G-linker-cdc12 pil1Δ::LgBiT fex1Δ fex2Δ ade6-M216 his3-D1 leu1-32 ura4-D18 h-* | Fig. 2b | Berro lab collection |
| SpJB1341 | *pil1Δ::LgBiT ent1-P571-Oakley-p1-LV-L3S-2G-HiBiT-2G-linker-ent1 fex1Δ fex2Δ ade6-M216 his3-D1 leu1-32 ura4-D18 h-* | Fig. 2f | Berro lab collection |
| SpJB1342 | *pil1Δ::LgBiT ent1-P571-Oakley-p1-2G-HiBiT-2G-linker-ent1 fex1Δ fex2Δ ade6-M216 his3-D1 leu1-32 ura4-D18 h-* | Fig. 2f | Berro lab collection |
| SpJB1371 | *pil1Δ::LgBiT ent1-P571-Oakley-p1-LV-L3S-2G-HiBiT-2G-linker-ent1-GSLIDL697AAAAAA, fex1Δ fex2Δ ade6-M216 his3-D1 leu1-32 ura4-D18 h-* | Fig. 2f | Berro lab collection |
| SpJB1443 | *sad1-mCherry rlc1-sfcherry2 cdc12-A216-DyneinStalk-IAAL-K3-cdc12 pil1Δ::NES_wis1-mEGFP-IAAL-E3 fex1Δ fex2Δ ade6-M216 his3-D1 leu1-32 ura4-D18 h-* | Fig. 2d | Berro lab collection |

## Supplementary Table S2

Nematode strain collection

| Strain ID | Genotype | Curator |
|---|---|---|
| Phx7438 | unc-70(syb7438[unc-70(1166R + $GFP_{11}$ + 1167D)]) (V) | Berro lab |
| Phx7460 | unc-70(syb7460[unc-70(1166R + 3pN-Sensor-$GFP_{11}$ + 1167D)]) (V) | Berro lab |
| Phx8023 | unc-70(syb8023[unc-70(1166R + 5pN-Sensor-$GFP_{11}$ + 1167D)]) (V) | Berro lab |
| Phx8051 | unc-70(syb8051[unc-70(1166R + 7pN-Sensor-$GFP_{11}$ + 1167D)]) (V) | Berro lab |
| Phx7442 | unc-70(syb7442[unc-70(1166R + 10pN-Sensor-$GFP_{11}$ + 1167D)]) (V) | Berro lab |
| MTS2374 | unc-70(syb7438[unc-70(1166R + $GFP_{11}$ + 1167D)]) (V); shyIs83 [Pmec-17::GFP1-10, Podr-1::RFP] (I) | Yogev lab |
| MTS2364 | unc-70(syb7460[unc-70(1166R + 3pN-Sensor-$GFP_{11}$ + 1167D)]) (V); shyIs83 [Pmec-17::GFP1-10, Podr-1::RFP] (I) | Yogev lab |
| MTS2665 | unc-70(syb8023[unc-70(1166R + 5pN-Sensor-$GFP_{11}$ + 1167D)]) (V); shyIs83 [Pmec-17::GFP1-10, Podr-1::RFP] (I) | Yogev lab |
| MTS2616 | unc-70(syb8051[unc-70(1166R + 7pN-Sensor-$GFP_{11}$ + 1167D)]) (V); shyIs83 [Pmec-17::GFP1-10, Podr-1::RFP] (I) | Yogev lab |
| MTS2375 | unc-70(syb7442[unc-70(1166R + 10pN-Sensor-$GFP_{11}$ + 1167D)]) (V); shyIs83 [Pmec-17::GFP1-10, Podr-1::RFP] (I) | Yogev lab |
| MTS2376 | unc-70(syb7460[unc-70(1166R + 3pN-Sensor-$GFP_{11}$ + 1167D)]) (V); shyIs83 [Pmec-17::GFP1-10, Podr-1::RFP] (I); *unc-115(ky275)* (X) | Yogev lab |
| MTS2377 | unc-70(syb7438[unc-70(1166R + $GFP_{11}$ + 1167D)]) (V); shyIs83 [Pmec-17::GFP1-10, Podr-1::RFP] (I); *unc-115(ky275)* (X) | Yogev lab |

**Supplementary Table S3**

DNA templates for nematode strains

The following DNA sequences served as templates generate the alleles syb7438, syb7460, syb8023, syb8051 and syb7442, which are endogenous insertions of the force sensors into unc-70/ß-spectrin. Strains were ordered from SunyBiotech.

| Construct | Sequence | Annotations |
|---|---|---|
| **GFP$_{11}$** (as in syb7438) | AACTTCTCAATCAACACGCTGCCATCCGTggtg gatcacgagatcacatggttctgcacgagtacgttaacgccgcgg gaatcacctcgggcggaGAAGA*A**ATTGACGGATAC GCTGAGGATTACAAGAAGATGCGTGCAATGG GAGATCGTGTCAC | genomic DNA (unc-70)<br>* Silent mutation<br>linker<br>GFP$_{11}$ |
| **3pN-Sensor GFP$_{11}$** (as in syb7460) | AACTTCTCAATCAACACGCTGCCATCCGTGG CGGCGGCGGCCTGAGAAAGATAAAAGAGAC TGTCGATCAAGTAGAAGAGCTCAGAAGAGCT CTTCGTATCAAATCGCAAGAGCTTGAAGTAAA AAATGCAGCGGCAAACGACAAACTCAAGAAG ATGGTGAAGGACCAACAAGAGGCCGAAAAAA AAAAAGTAATGTCACAAGAAATTCAAGAGCAG CTTCATAAACAACAGGAAGTCATCGCTGACA AGCAGATGTCAGTGAAAGAGGATTTAGACAA GGTAGAGggtggatcacgagatcacatggttctgcacgagta cgttaacgccgcgggaatcacctcgggcggaCTGCGTAAC GAGCTTCAGAAGTTGGAGGACGATGCTAAAG ACAACCAACAAAAAGCTAACGAAGTAGAACA GATGATACGTGACTTAGAAGCCAGTATAGCG CGATACAAAGAGGAGTATGCTGTTTTGATCTC AGAGGCGCAGGCTATAAAGGCAGACCTGGC GGCGGTCGAGGCGAAAGTTAATAGAAGTACA GCCCTTCTTAAATCTCTTAGTGCCGAGCGTG AGCGATGGGAGAAAACGAGTGGTGGAGGTG GAGAAGA*A**TTGACGGATACGCTGAGGATT ACAAGAAGATGCGTGCAATGGGAGATCGTGT CAC | genomic DNA (unc-70)<br>* Silent mutation<br>coiled coil (3 pN sensor)<br>linker<br>GFP$_{11}$ |
| **5pN-Sensor GFP$_{11}$** (as in syb8023) | AACTTCTCAATCAACACGCTGCCATCCGTGG TGGAGGCGGCGCTCAATCGGAGAAAGAGGT TCAAGCCTTGGAGAAAAAGGTTGCGCAATTA GAATGGGAAAATCAAGCACTTGAAAAAGAAG TGGCACAGggtggatcacgagatcacatggttctgcacgag tacgttaacgccgcgggaatcacctcgggcggaGCTCAAGT GAAAAAAAAGTTACAGGCAAATAAGAAAGAG CTTGCTCAAGTAAAATGGAAGCTCCAAGCCG TCAAAAAGAAGTCAGCTCAGGGAGGAGGCG | genomic DNA (unc-70)<br>* Silent mutation<br>Coiled coil 5pN sensor<br>linker<br>GFP$_{11}$ |

| | | |
|---|---|---|
| | GTGAAGAGATTGACGGATACGCTGAGGATTACAAGAAGATGCGTGCAATGGGAGATCGTGTCAC | |
| **5pN-Sensor GFP$_{11}$** (as in syb8051) | AACTTCTCAATCAACACGCTGCCATCCGTGGAGGAGGTGGAGCACAACTGGAGAAAGAGCTCCAGGCGCTCGAAAAGAAACTCGCCCAATTGGAATGGGAAAATCAGGCTTTGGAGAAAGAACTTGCACAAggtggatcacgagatcacatggttctgcacgagtacgttaacgccgcgggaatcacctcgggcggaGCGCAATTAAAGAAAAAACTCCAGGCAAATAAAAAAGAATTAGCCCAATTGAAATGGAAACTCCAGGCCTTGAAGAAAAAATTAGCGCAAGGTGGAGGTGGAGAAGAGATTGACGGATACGCTGAGGATTACAAGAAGATGCGTGCAATGGGAGATCGTGTCAC | genomic DNA (unc-70)<br>* Silent mutation<br>Coiled coil 7pN sensor<br>GFP$_{11}$ |
| **10pN - Sensor GFP$_{11}$** (as in syb7442) | AACTTCTCAATCAACACGCTGCCATCCGTGGTGGTGGCGGAGCGCAATTGGAAAAGGAACTTCAGGCACTGGAAAAAAAGCTGGCGCAACTTGAGTGGGAGCTCCAAGCTCTGGAGAAAGAGAATGCCCAGCTGGAAAAGGAGCTCCAAGCTggtggatcacgagatcacatggttctgcacgagtacgttaacgccgcgggaatcacctcgggcggaCAGGCTCTGAAGAAGAAGTTGGCGCAGAACAAGAAGAAACTCCAAGCGTTAAAGAAAGAGCTTGCACAGTTAAAATGGAAGCTTCAAGCGCTCAAGAAGAAATTAGCCCAAGGTGGCGGCGGAGAAGAA*ATTGACGGATACGCTGAGGATTACAAGAAGATGCGTGCAATGGGAGATCGTGTCAC | genomic DNA (unc-70)<br>* Silent mutation<br>coiled coil (10 pN sensor)<br>linker<br>GFP$_{11}$ |

**Supplementary Table S4**

**Sequences of calibrated coiled-coils. Linkers are underlined.**

cc-3 pN:
GGGGLRKIKETVDQVEELRRALRIKSQELEVKNAAANDKLKKMVKDQQEAEKKKVMS
QEIQEQLHKQQEVIADKQMSVKEDLDKVEGGSSGGLRNELQKLEDDAKDNQQKANEV
EQMIRDLEASIARYKEEYAVLISEAQAIKADLAAVEAKVNRSTALLKSLSAERERWEKTS
GGGG

cc-5 pN:
GGGGAQSEKEVQALEKKVAQLEWENQALEKEVAQGGSSGGAQVKKKLQANKKELAQ
VKWKLQAVKKKSAQGGGG

cc-7 pN:
GGGGAQLEKELQALEKKLAQLEWENQALEKELAQGGSSGGAQLKKKLQANKKELAQL
KWKLQALKKKLAQGGGG

cc-10 pN:
GGGGAQLEKELQALEKKLAQLEWELQALEKENAQLEKELQAGGSSGGQALKKKLAQN
KKKLQALKKELAQLKWKLQALKKKLAQGGGG

cc-11 pN:
GGGGAQLEKELQALEKKLAQLEWENQALEKELAQLEKELQALEKELAQGGSSGGAQL
KKKLQALKKKLAQLKKKLQANKKELAQLKWKLQALKKKLAQGGGG

cc-13 pN:
GGGGAQLEKELQALEKKLAQLEWENQALEKELAQLEKELQALEKELAQLEKELQALEK
ELAQGGSSGGAQLKKKLQALKKKLAQLKKKLQALKKKLAQLKKKLQANKKELAQLKWK
LQALKKKLAQGGGG

# Supplementary figures

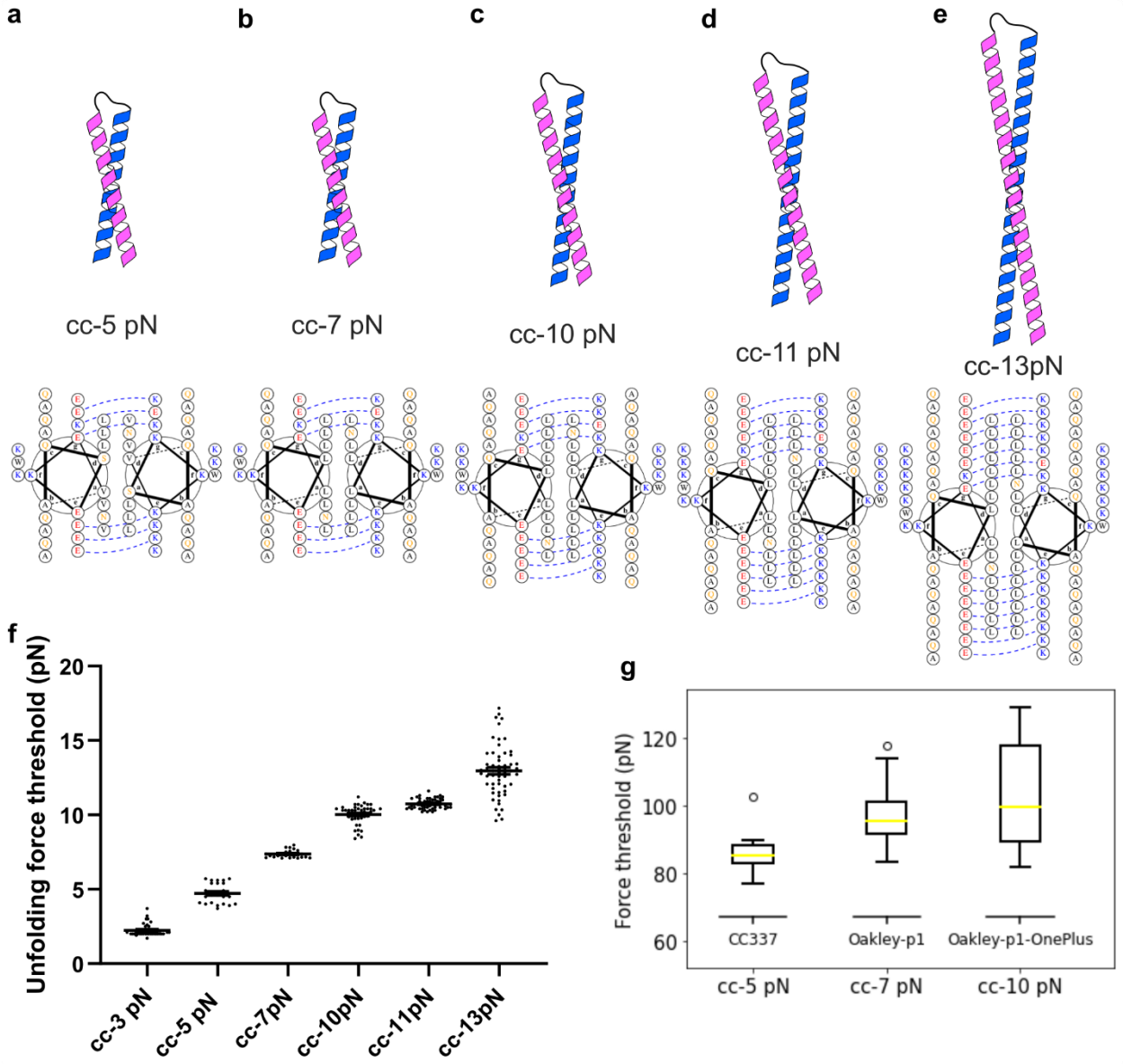


**Figure S1. Design of heterodimeric anti-parallel coiled-coils. a-e**, Schematics of cc-5 pN, cc-7 pN, cc-10 pN, cc-11 pN and cc-13 pN with their sequences shown as helical wheels (https://grigoryanlab.org/drawcoil/). E/K electrostatic charges are paired by dotted lines. Mechanical stabilities are tuned by mutating the hydrophobic core (amino acids in positions *a* and *d*) and by changing the total number of heptads. **f**, Unfolding force thresholds of coiled-coils calibrated by optical traps. Each dot represents a pulling event. **g**, Unfolding force thresholds of coiled-coils from simulation. MD simulation can be used to guide coiled-coil design but cannot predict the exact values. See materials and methods for details.

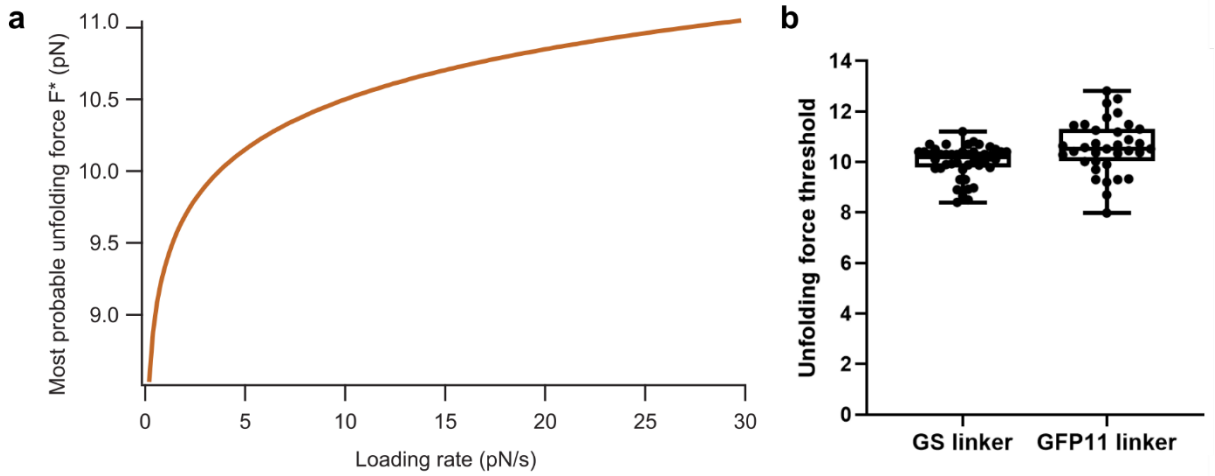


**Figure S2. Changes in the force loading rate or the linker have negligible influence on coiled-coil unfolding force threshold a**, The most probable unfolding force F* as a function of the force loading rate was calculated as described previously[26]. Given the approximate force loading rate of 2.3 pN/s *in vivo* and the force loading rate of ~1.2 pN/s in optical tweezer experiments[14,15,62,64], the difference in the unfolding force of cc-10pN reported *in vitro* and *in vivo* is less than 1 pN. The difference in the unfolding force of cc-10pN between 1 pN/s and 30 pN/s is less than 2 pN. **b**, Changing the linker of cc-10 pN from a GS linker (GGSSGG) to GFP11 linker (GGRDHMVLHEYVNAAGITGG) does not significantly change the unfolding force threshold.

**Figure S3. Titration of cells and substrates for luminescence measurement. a**,

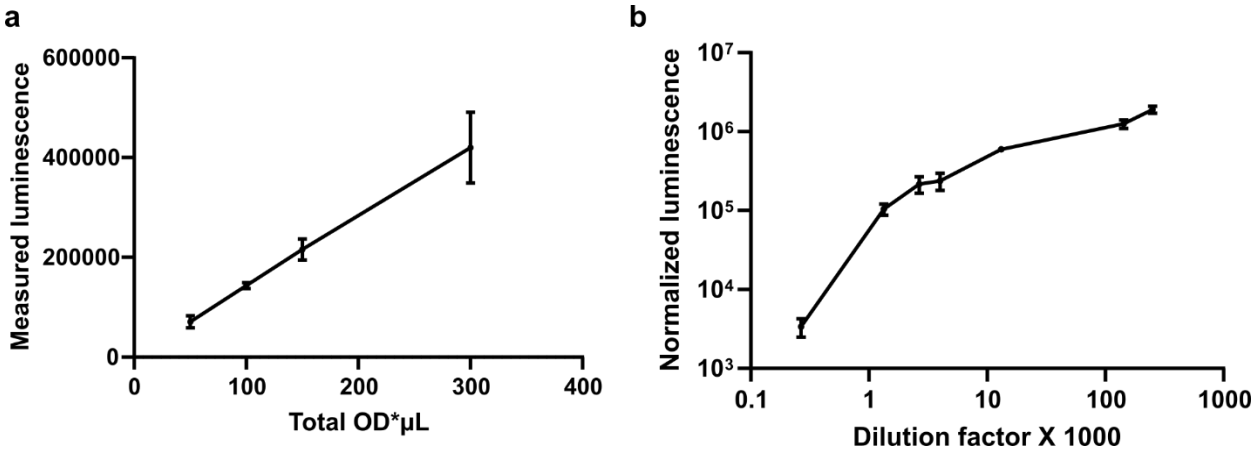


Correlation between the total luminescence of fission yeast cells and the number of cells, represented by total OD* µL (1 OD* µL corresponds to $10^4$ cells). Substrates (Nano-Glo Live) were diluted 1:11. **b**, Correlation between normalized luminescence from fission yeast cells and the dilution of substrates. 100 OD* µL cells were used for each measurement, and the luminescence readings were normalized by the OD measurements on the plate reader. Error bars are SEM. The total number of cells and the

dilution of substrates were kept constant for strains expressing LgBiT and coiled-coil force sensors with HiBiT linker.

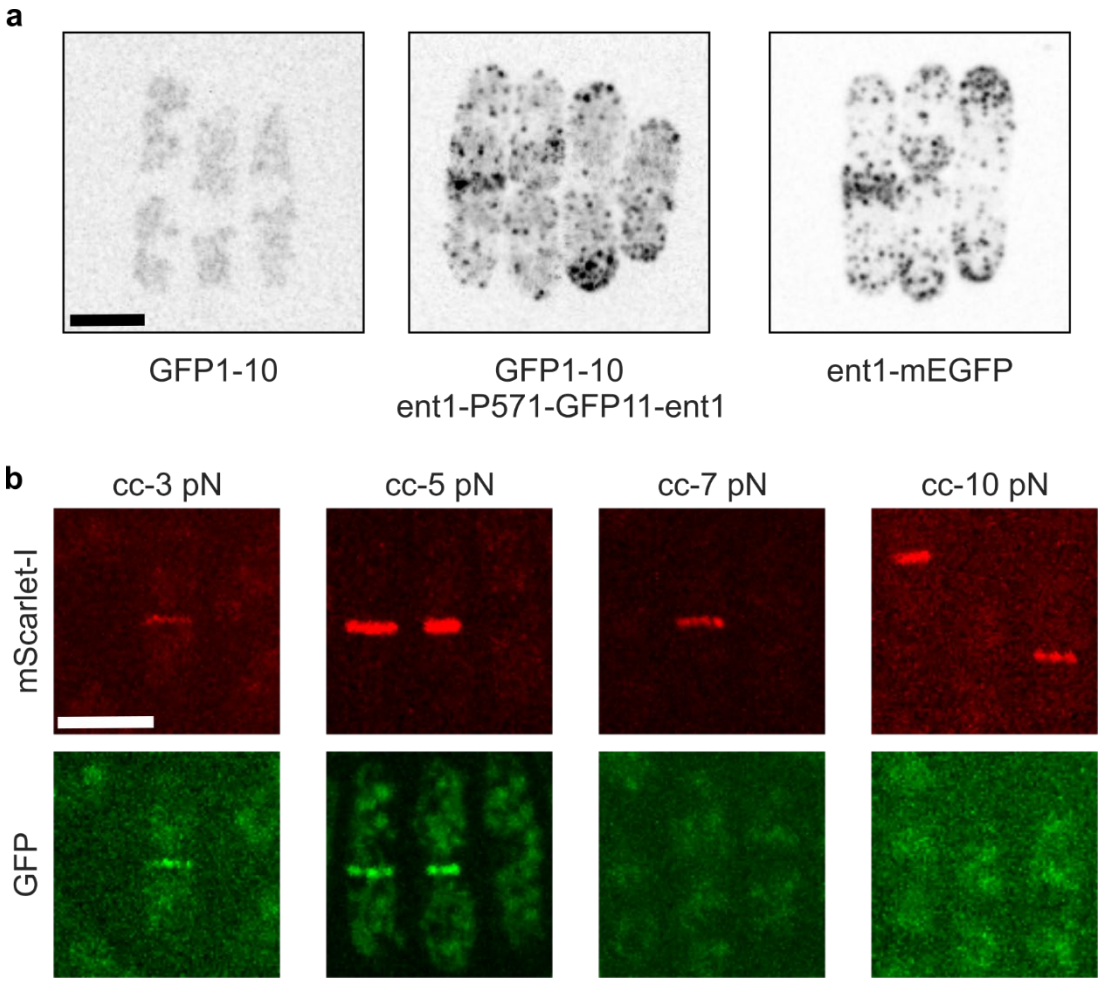


**Figure S4. Force measurement with split-GFP readout in the fission yeast. a**, Fission yeast cells expressing GFP1-10 alone have weak fluorescent signals (left image). Co-

expression of GFP1-10 and GFP11 (inserted after P571 in Ent1, middle image) led to GFP reconstitution and the appearance of fluorescent signals similar to Ent1-mEGFP (right image) in pattern but with decreased intensity. Images are max projected whole cell sections acquired and displayed with the same settings. **b**, Quantification of forces on Cdc12 with the split-GFP readout. In cells expressing GFP1-10, endogenous Cdc12 was tagged with mScarlet-I for visualization. Force sensors (cc-3 pN, cc-5 pN, cc-7 pN, or cc-10 pN) with GFP11 linker were inserted into Cdc12 after A216, and the GFP signals were normalized with respect to mScarlet-I signals to quantify force on Cdc12. Scale bars, 5 μm.

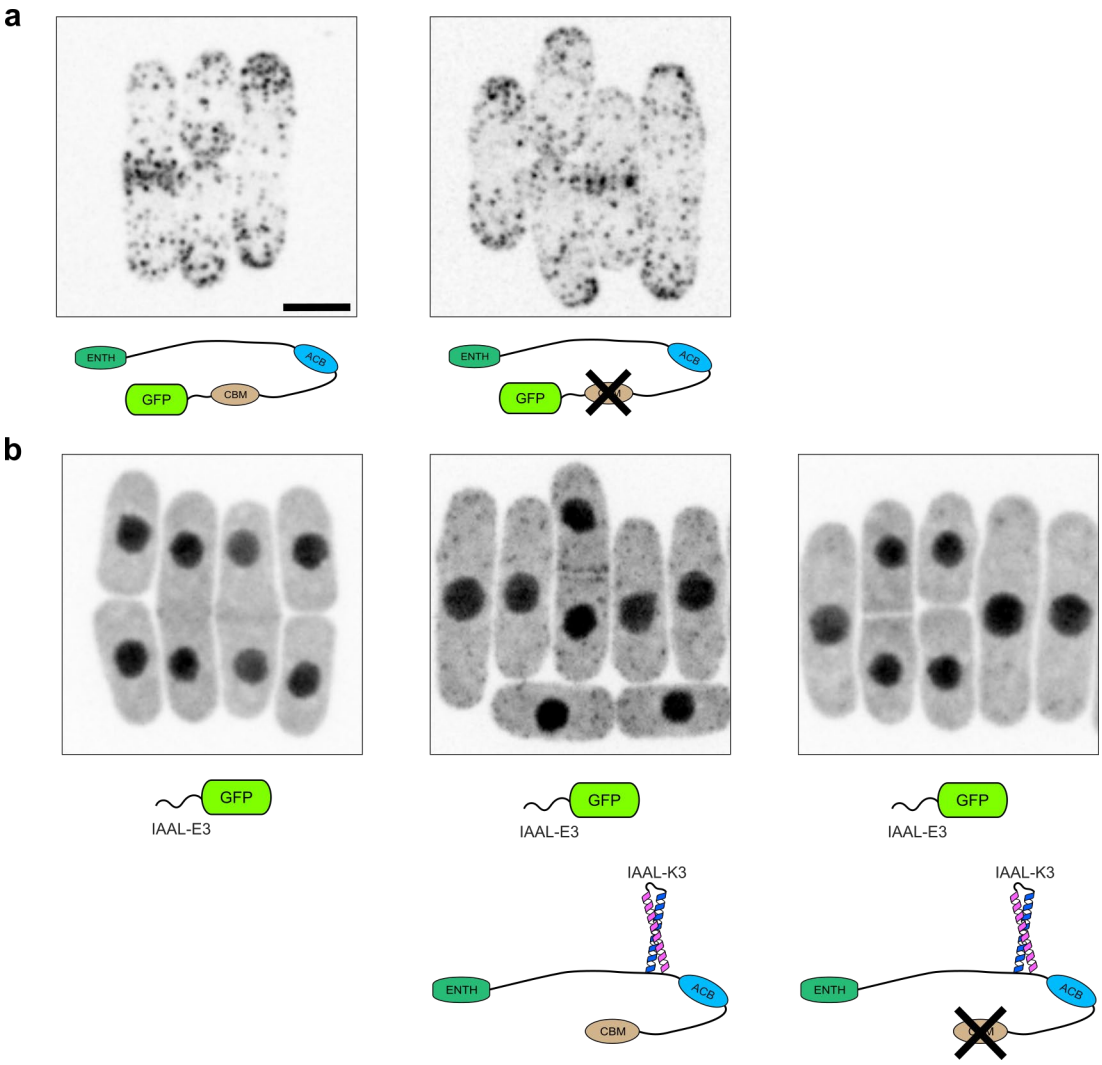


**Figure S5. Deletion of the clathrin-binding motif (CBM) reduces the force on Ent1.** **a**, The subcellular localization of Ent1 is visualized by GFP tagging. Deletion of CBM does not change the endocytic localization of Ent1. **b**, mEGFP-IAAL-E3 binder is enriched at endocytic sites in cells where cc-3 pN with IAAL-K3 linker is inserted into Ent1, indicating that force on Ent1 is above 3 pN in wild type cells. The deletion of CBM reduces force on Ent1 and led to the disappearance of locally enriched fluorescent signals. Images are max projected whole cell sections acquired and displayed with the same settings. Schematics below each image indicate the genotype of each strain. Scale bar, 5 μm.

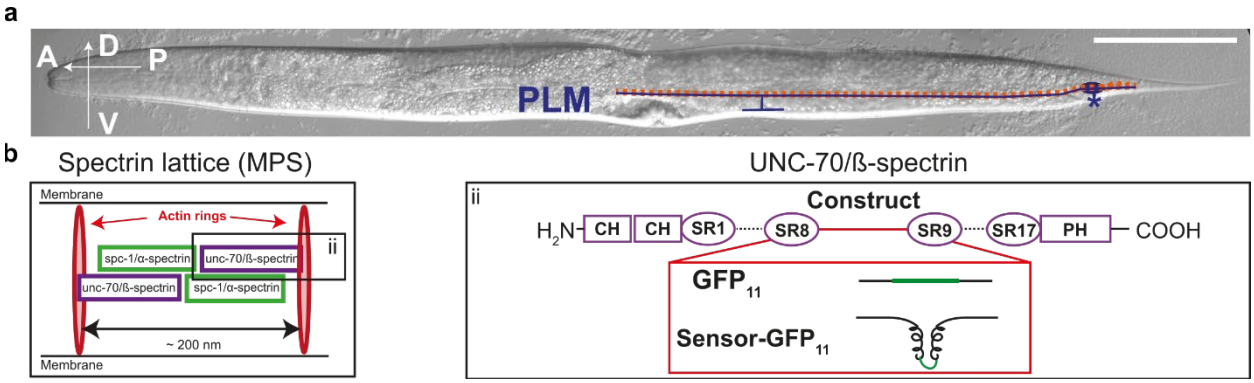


**Figure S6. Insertion of force sensors into UNC-70 in *C. elegans*. a**. Position of the sensory PLM neuron (blue) is illustrated in a DIC image of a nematode. Coordinates on the left show the anterior-posterior (A, P) and ventral-dorsal (V,D) axis. The PLM cell body (*) is located close to the tail of the nematode where it extends a short neurite posterior towards the tail and a long neurite anterior towards the center of the animal. Along this anterior neurite, PLM forms a short branch to innervate interneurons in the ventral nerve cord. The red dashed line along the entire length of the neurites indicates the analyzed region for Fig. 2j-k. Scale bar, 100 µm. **b**. Left panel: Spectrins form the central building block of the membrane-associated periodic skeleton (MPS), which consists of actin rings that are interspaced by spectrin tetramers and form a periodic lattice below the plasma membrane throughout the entire length of the axon. Each spectrin tetramer spaces a length of approximately 200 nm and consists of two heterodimers of α- (SPC-1 in nematodes) and ß-spectrin (UNC-70 in nematodes) subunits, that assemble head-to-head. Right panel: Protein domain organization in UNC-70/ß-spectrin with location of the tension probe insertion. A tension sensor or GFP11 alone (control) were inserted into the genomic unc-70 locus at the position that encodes for the linker region between spectrin repeats 8 and 9 (after R1167). CH: Calponin Homology Domain, SR: Spectrin-like Repeats, PH: Pleckstrin Homology Domain.

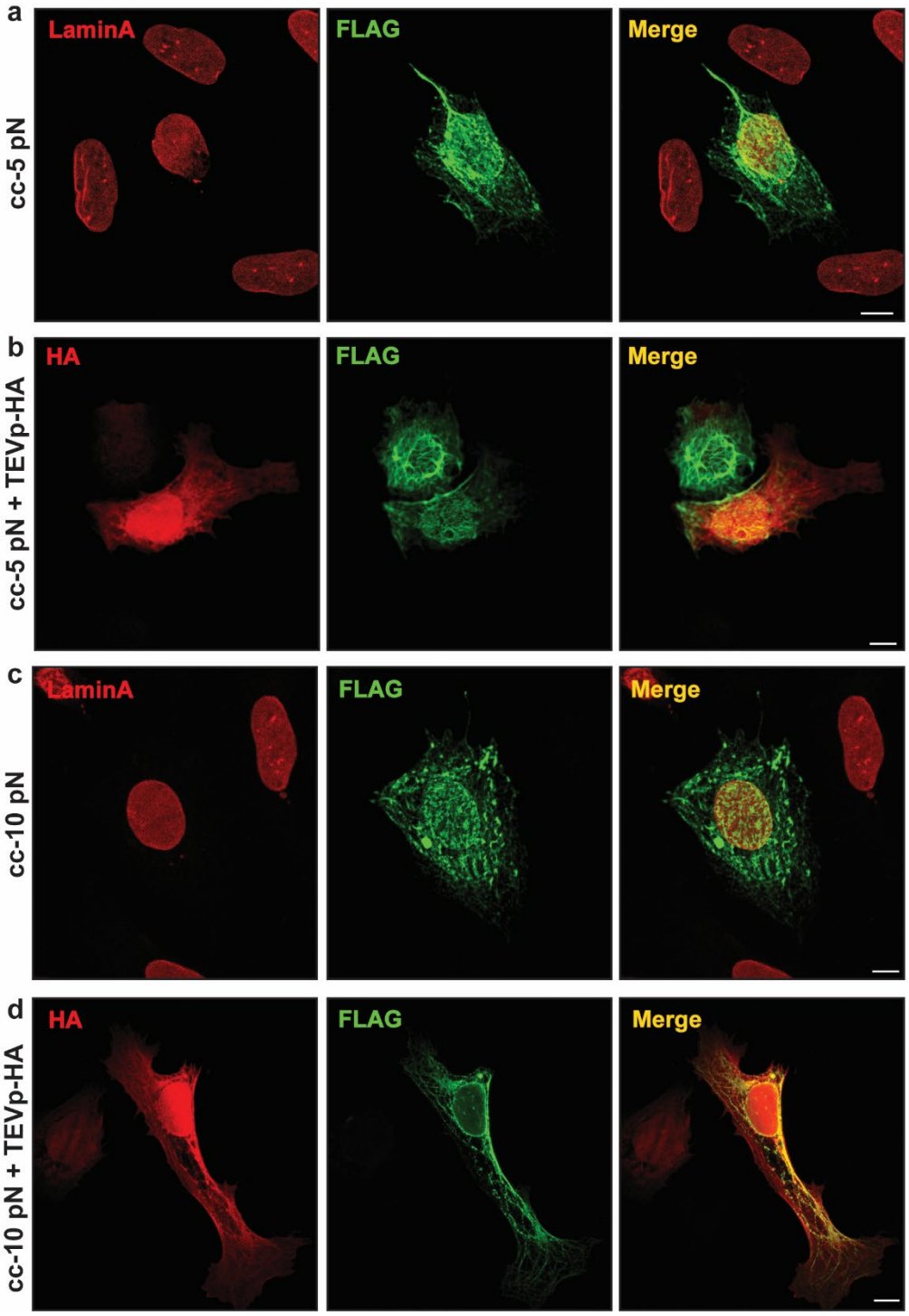


**Figure S7. Force measurements on mini-Nesprin-2G with TEV cleavage system. a-d**, Representative immunofluorescence images of U2OS cells expressing the mini-Nesprin-2G protein with the indicated force sensors cc-5 pN (a, b) and cc-10 pN (c, d) either without (a, c) or with (b, d) TEVp-HA co-expressed. Scale bar, 10 μm.

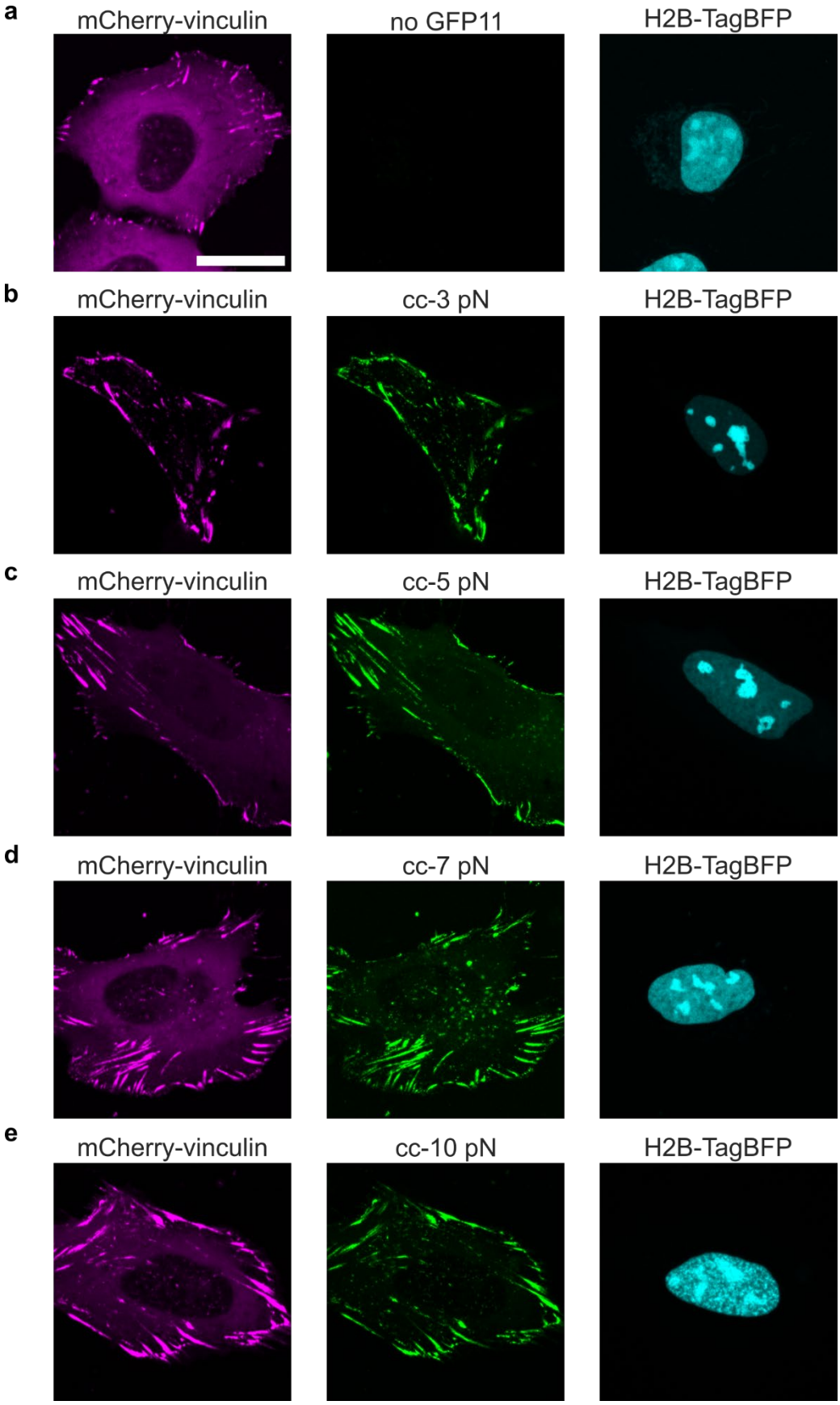

**S8. Force measurement on vinculin with split-GFP readout. a**, U2OS cells expressing mCherry-vinculin and H2B-TagBFP-P2A-GFP1-10 (H2B-TagBFP signal was used as an equimolar expression marker for GFP1-10) were imaged on a confocal microscope. No GFP signal was detected in cells lacking GFP11. **b-e**, U2OS cells expressing mCherry-vinculin with different force sensors inserted after E883, and expressing H2B-TagBFP-P2A-GFP1-10 from a co-transfected plasmid. The appearance of GFP signals indicate forces above the unfolding threshold of each coiled-coil sensor. The ratio between GFP and mCherry fluorescence was used as an index to quantify forces on vinculin molecules in Fig. 2p. Scale bar, 20 μm.